



HAL
open science

Evidence for a persistent magma reservoir with large melt content beneath an apparently extinct volcano

Mickaël Laumonier, O. Karakas, O. Bachmann, Fabrice Gaillard, R. Lukacs, I. Seghedi, Thierry Menand, S. Harangi

► **To cite this version:**

Mickaël Laumonier, O. Karakas, O. Bachmann, Fabrice Gaillard, R. Lukacs, et al.. Evidence for a persistent magma reservoir with large melt content beneath an apparently extinct volcano. *Earth and Planetary Science Letters*, 2019, 521, pp.79-90. 10.1016/j.epsl.2019.06.004 . hal-02163470

HAL Id: hal-02163470

<https://uca.hal.science/hal-02163470>

Submitted on 9 Dec 2019

HAL is a multi-disciplinary open access archive for the deposit and dissemination of scientific research documents, whether they are published or not. The documents may come from teaching and research institutions in France or abroad, or from public or private research centers.

L'archive ouverte pluridisciplinaire **HAL**, est destinée au dépôt et à la diffusion de documents scientifiques de niveau recherche, publiés ou non, émanant des établissements d'enseignement et de recherche français ou étrangers, des laboratoires publics ou privés.

Evidence for a persistent magma reservoir with large melt content beneath an apparently extinct volcano

M. Laumonier^{1*}, O. Karakas², O. Bachmann², F. Gaillard³, R. Lukács⁴, I. Seghedi⁵, T. Menand¹, S. Harangi^{4,6},

¹Université Clermont Auvergne, CNRS, IRD, OPGC, Laboratoire Magmas et Volcans, F-63000 Clermont-Ferrand, France

²Department of Earth Sciences, Institute of Geochemistry and Petrology, ETH Zurich, Switzerland

³Université d'Orléans, CNRS, BRGM, ISTO, UMR 7327, F -45071, France

⁴MTA-ELTE Volcanology Research Group, Budapest, Hungary

⁵Institute of Geodynamics, Romanian Academy, Bucharest, Romania

⁶Eötvös Loránd University, Department of Petrology and Geochemistry, Budapest, Hungary

*corresponding author: mickael.laumonier@gmail.com

Keywords

Seemingly inactive volcano; Magma storage; numerical simulation; mush petrology; in-situ electrical-conductivity measurement; geophysical interpretation.

Highlights

- Petrological observations imply a trans-crustal magmatic system beneath Ciomadul
- Thermal evolution of such magmatic system is consistent with melt persistence
- Electrical measurements confirm the presence of 20-58% of hydrous melt under Ciomadul
- Ciomadul has a long-term subvolcanic magma storage above the solidus
- Volcano status must be defined based on the magmatic reservoir storage conditions

Abstract

Most active volcanoes display eruption frequencies of 10-1000s years but a class of volcanic systems has extremely long repose-time (>10's kyr), and are deemed as extinct. Yet, some reawaken, posing a particular threat because little is known about the way they endure and stir back to life. Reawakening primarily depends on the nature of the subvolcanic magma reservoir, especially the presence and distribution of melt. Here, we integrate petrology, thermobarometry, thermomechanical models, geophysics and *in situ* electrical conductivity measurements to show that the magma storage beneath Ciomadul, a seemingly inactive volcano in eastern-central Europe that last erupted 30 ka, may still hold 20 to 58 km³ of water-rich silicic melt, constituting up to 20-58 % in parts of the upper crustal crystal mush body. Such a melt volume exceeds the volume of erupted lava over the entire history of the volcano. This illustrates the important longevity of a magmatic reservoir at temperature above the solidus, which implies that there is still a potential for rapid mush rejuvenation. That a seemingly dead volcano like Ciomadul is actually capable of erupting in the future calls for renewed attention to "inactive" volcanoes worldwide and perhaps for a redefinition of their activity/inactivity status.

43 **1. Introduction**

44 **1.1. Magma storage beneath volcanoes**

45 Magma reservoirs beneath volcanoes are considered to subsist dominantly at high crystallinity
46 (Annen et al., 2006; Bachmann and Huber, 2016; Cashman et al., 2017) (“crystal mush”), surviving
47 over 10’s or 100’s thousands of years (Bachmann, 2010; Cooper, 2015; Costa, 2008; Gelman et al.,
48 2013) as they are episodically replenished by magma influx from below (Annen et al., 2006; Karakas
49 et al., 2017). Within these bodies, melt-dominated (> ~50% melt) regions, *i.e.* magma chambers, can
50 form and feed volcanic activity. However, due to difficulties in detecting and probing such molten
51 bodies at depth, the magma storage conditions are still debated based on three main hypotheses:
52 reservoirs (1) contain a significant amount of melt for long periods of time (Barboni et al., 2016), (2)
53 remain dominantly just above the solidus at relatively low melt fraction, with some small melt-rich
54 pockets periodically forming by extraction from the much larger surrounding mush zone (Cooper,
55 2019; Szymanowski et al., 2017) or (3) they are stored dominantly in subsolidus state (Cooper, 2019;
56 Rubin et al., 2017). Existence and distribution of melt in the storage zone greatly affects the
57 reactivation potential of a magma body (Huber et al., 2011) and defines the nature of a volcano, *i.e.*
58 whether it is still potentially active or considered extinct. In this context, the prolonged preservation
59 of significant melt fractions in the storage region has a particular importance, and its detection and
60 description is crucial to assess the level of potential volcanic hazards.

61 Ciomadul, located in eastern-central Europe (Fig. 1) is an excellent example of a seemingly inactive
62 volcano (Harangi et al., 2015a; Szakács et al., 2015), because its eruption chronology shows long
63 quiescence periods (Molnár et al., 2018) between active phases, with its last eruption occurring
64 around 30 ka (Harangi et al., 2015a; Karátson et al., 2016; Molnár et al., 2019). It consists of fairly
65 homogeneous high-K dacites, but contains complexly zoned crystals of plagioclase, amphibole and
66 biotite (Harangi et al., 2015b). Although Ciomadul has been in a seemingly inactive state for a long
67 time, several lines of evidence support a long-lived system holding a potentially active magma

68 storage (Harangi et al., 2015a, 2015b) (“PAMS” volcano): (1) significant CO₂-emanations with strong
69 magmatic component (Kis et al., 2019), (2) wide range of zircon crystallization ages (from 60 ka to
70 350 ka) suggestive of a long-lived system till today(Harangi et al., 2015a) and (3) petrological
71 evidences for the presence of felsic crystal mush and open-system magmatic processes in the
72 magma storage(Harangi et al., 2015b; Kiss et al., 2014). Furthermore, (4) geophysical anomalies such
73 as low electrical resistivity and seismic wave attenuation were observed from the base of the crust
74 and may reveal the subvolcanic plumbing system(Harangi et al., 2015b; Popa et al., 2012). The
75 magnetotelluric survey evidenced a conductive body from about 5 to 27 km depth with a particularly
76 high signal between 9 and 21 km depth(Harangi et al., 2015b) (electrical resistivity < 2 ohm.m). Such
77 anomaly is consistent with the existence of a magma reservoir in the middle to upper crust, but this
78 shallow conductor makes it difficult to resolve potential underlying features (Bedrosian, 2007). From
79 geophysics, it is thus uncertain whether there is a continuous mushy zone down to the lower crustal
80 hot zone or not. The status of Ciomadul’s plumbing system, *i.e.* the existence and amount of melt,
81 cannot be elucidated solely from geophysical observations; petrological data could also help to
82 reveal the trans-crustal magmatic system(Cashman et al., 2017) beneath Ciomadul, as it has been
83 suggested for other magma storage systems around the world(Bachmann and Huber, 2016;
84 Christopher et al., 2015).

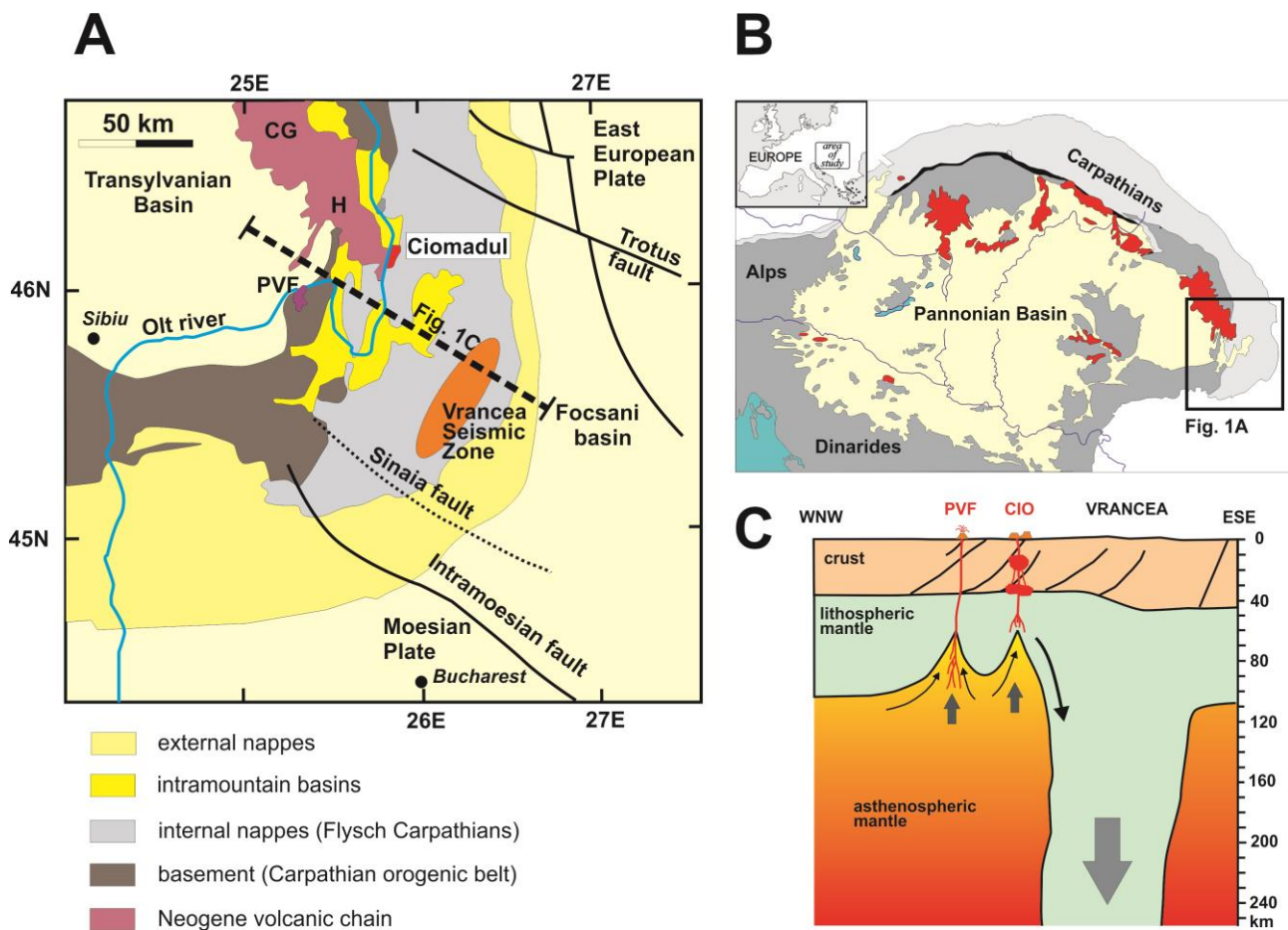
85 In order to better constrain the current state of Ciomadul volcano, we propose a direct modelling
86 of the geophysical signal of its plumbing system: a petrological analysis is used to build numerical
87 simulations of the thermal evolution of the magmatic reservoir that is converted into electrical
88 conductivity distribution. The integration of this modelling with geophysical observations indicates
89 that a significant amount of water-rich silicic melt (at minima 15%) must still be present in the upper
90 crust beneath the volcano, implying that the reservoir is likely to have been kept in warm enough
91 conditions to preserve sizeable domains in near-eruptible state. This calls for attention about long-

92 dormant volcanoes and questions the definition of potentially active, dormant and extinct
93 volcanoes (Szakács, 1994), since their plumbing systems may be comparable to active volcanoes.

94

95 **1.2. Geological settings of Ciomadul Volcano**

96 Ciomadul is located at the southern edge of the ca. 160 km long Calimani-Gurghiu-Harghita volcanic
97 chain, and represents the latest manifestation of the Neogene to Quaternary volcanism in the post-
98 collisional tectonic setting of the Carpathian-Pannonian Region (Fig. 1) (Harangi and Lenkey, 2007;
99 Seghedi and Downes, 2011). The volcanism of Ciomadul occurred in a geodynamically still active
100 region, close to the Vrancea area, where a near-vertical lithospheric slab descending in the upper
101 mantle causes frequent deep-hypocentres (70-170 km) earthquakes (Ismail-Zadeh et al., 2012). The
102 latest eruptions for the last 1 Myr (Molnár et al., 2018) formed a volcanic dome field consisting of
103 small volume ($<0.5 \text{ km}^3$) lava domes and the massive Ciomadul volcanic complex ($8-14 \text{ km}^3$). The
104 Ciomadul volcanic complex is the amalgamation of several lava domes truncated by two explosive
105 craters developed from 160 ka to 30 ka (Harangi et al., 2015a; Karátson et al., 2016; Molnár et al.,
106 2019; Szakács et al., 2015).



107

108

109

110

111

112

113

114

115

116

117

118

119

120

121

Figure 1: Geological context of Ciomadul volcano. (A) Location of the Ciomadul volcanic complex in the southeastern Carpathian area of the Carpathian-Pannonian Region (simplified geological map after Cloetingh et al., 2004 and Martin et al., 2006). CG=Călimani-Gurghiu volcanic complex, H=Harghita volcanic complex, PVF = Perșani Volcanic Field. (B) The study area in Europe and in the Carpathian-Pannonian region with the surface exposures of the Miocene to Quaternary calc-alkaline andesitic to dacitic volcanic areas (red colour). (C) Cross section through the Quaternary volcanic areas and the Vrancea seismic zone showing conceptual model for lower lithospheric ruptures due to the downgoing vertical lithospheric slab beneath the Vrancea Zone (modified after Seghedi et al., 2011; PVF = Perșani Volcanic Field; CIO = Ciomadul Volcanic Complex).

2. Samples and methods

2.1. Starting material

The pumiceous dacite studied experimentally to determine the electrical conductivity belongs to one of the youngest eruptions of the Ciomadul (30 ka; Bixad locality; (Harangi et al., 2015a, 2010; Vinkler et al., 2007)). It represents a hot block-and-ash flow deposit formed either by fountain

122 collapse of a Vulcanian explosion event such as occurred at Soufriere Hills, Montserrat in 1997 or
 123 explosive destruction of a growing lava dome (Vinkler et al., 2007). The bulk composition is high-K
 124 dacite typical of other volcanic products of Ciomadul (Molnár et al., 2018; Vinkler et al., 2007) (Table
 125 1); it has relatively high Na₂O (>4.2 wt%) and K₂O (>3 wt%) contents, whereas the trace element
 126 composition is characterized by abundance of Ba and Sr (both elements are above 1500 ppm),
 127 depletion of Y (<10 ppm) and heavy rare earth elements (Yb <1 ppm; Lu<0.15 ppm). The dacite has
 128 a vesiculated glassy groundmass with ca. 30 vol.% phenocrysts of plagioclase, amphibole and biotite
 129 (see additional information in Results section). In the dome rocks, crystal clots frequently occur;
 130 they are mostly felsic (plagioclase and amphiboles in addition to accessory minerals, while some of
 131 them contain also quartz, K-feldspar and Fe-Ti oxides) and most of them contain interstitial vesicular
 132 glass. Furthermore, the dome rocks usually contain high-Mg minerals, such as olivine, clinopyroxene
 133 and orthopyroxene, both as solitary crystals and crystal clots. Their high mg-numbers (>85) indicate
 134 origin from less differentiated basaltic magma (Kiss et al., 2014; Vinkler et al., 2007). The
 135 monotonous chemical and petrologic natures of the erupted dacites at Ciomadul and volcanic
 136 neighbours over the past 1 Myr (Molnár et al., 2018) suggest a rather uniform petrogenesis.

137

	SiO ₂	TiO ₂	Al ₂ O ₃	FeO	MnO	MgO	CaO	Na ₂ O	K ₂ O	P ₂ O ₅	Total
Vinkler et al., 2007	65.41	0.36	16.93	2.75	0.05	2.32	4.26	4.58	3.15	0.18	99.99
Vinkler et al., 2007	65.19	0.36	16.99	2.72	0.06	2.39	4.07	4.74	3.3	0.17	99.99
This study	65.79	0.35	16.77	2.10	0.06	2.09	3.83	4.73	3.41	nd	99.12
	<i>0.35</i>	<i>0.05</i>	<i>0.18</i>	<i>0.10</i>	<i>0.04</i>	<i>0.09</i>	<i>0.08</i>	<i>0.14</i>	<i>0.11</i>	<i>nd</i>	<i>0.47</i>

138 **Table 1: Bulk chemical composition (in wt%) of the Ciomadul dacite** determined by ICP-MS method (Vinkler et al.,
 139 2007) and of the dry starting glass (30 analyses) after melting of the Ciomadul sample determined by Electronic
 140 MicroProbe Analysis (standard deviation in italic font).

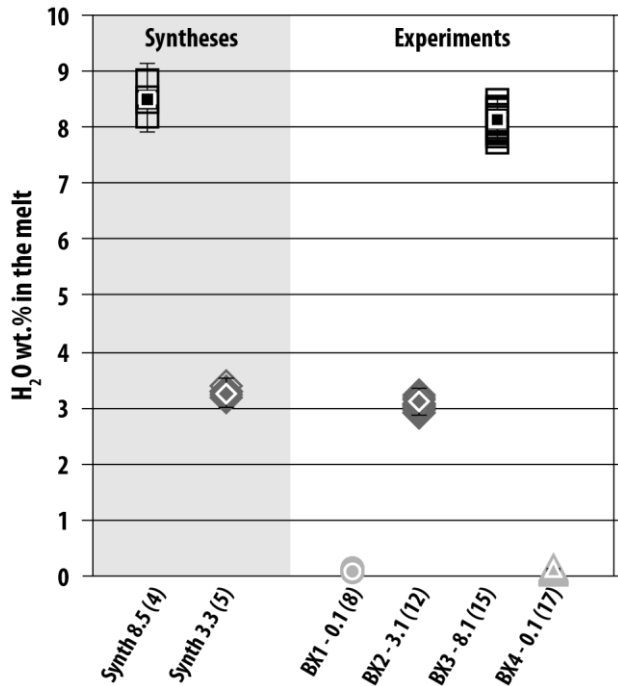
141

142 The chosen dacite sample as starting material (BX08 (Harangi et al., 2015b)) is regarded as
 143 representative of potential magma nowadays residing in the subvolcanic system for the following

144 reasons: (i) the dacite is the dominant eruption product and it represents the latest eruption phase
145 (Harangi et al., 2015a), (ii) it contains relatively low amount of phenocrysts (< 30%), suggesting that
146 its bulk composition is close to the last melt composition before extraction from the reservoir and
147 eruption, (iii) it does not contain significant amount of felsic crystal clots representing the cold
148 crystal mush nor high-Mg mafic minerals (olivine and pyroxene) that represent fragments of mafic
149 recharge.

150 The natural sample was crushed and fused at 1450°C under atmospheric conditions for 3 hours
151 twice to ensure chemical homogeneity (Table 1). The resulting glass was crushed again and used
152 either to constitute the dry samples, or after hydration (with appropriate mass of water added) in
153 piston cylinder to produce 3.1 and 8.1 wt.% water samples. Hydration syntheses were performed in
154 welded shut gold palladium capsules at 1.5 GPa and 1300°C and held for 2 days to ensure a
155 homogeneous water content.

156 The water concentration in synthetic glass and experimental products was measured by infra-red
157 spectroscopy at ISTO (Microscope IR Continuum coupled with a Nicolet 6700 spectrometer and a
158 MCT detector, Orleans, France) using KBr beam splitter. Each measurement consisted of 128 scans
159 with a resolution of 4 cm⁻¹. The two hydrated syntheses and the post experimental glasses (dry and
160 hydrous) were analyzed through 4 to 17 spots to check for homogeneity of the water concentration
161 (Fig. 2). We calculated the water concentration using the Beer–Lambert law, with density and
162 extinction coefficients from the literature (Ohlhorst et al., 2001), and the peak height absorbance
163 corrected by a linear baseline. The thickness of the sample was measured by the calibrated stage of
164 the microscope with an accuracy of less than 3 micrometers. To determine the water concentration
165 of the water rich glasses (> 8 wt.%), we used the molecular water (5200 cm⁻¹) and OH- (4500 cm⁻¹)
166 stretching vibrations. The water content of “dry” glasses and glasses with ~3wt.% of water were
167 measured using the fundamental H₂O-stretching vibration (3530 cm⁻¹). The propagated uncertainty
168 results in a maximal error in [H₂O] of 0.5 wt.%(Laumonier et al., 2017b).



170

171 **Figure 2: Water content of dacitic glasses** after hydration (Syntheses) and of experimental glasses after electrical
 172 conductivity measurements ("Experiments"). Empty symbols correspond to single analyses and full symbols to the
 173 average. The water variation before and after *in situ* electrical conductivity experiments is neglectable (lower than 5%).

174

175 2.2. Numerical simulation of the thermal evolution of Ciomadul upper reservoir

176 We used a two-dimensional thermal model modified from Karakas and Dufek (2015) and Karakas et
 177 al. (2017) and quantified the magma evolution beneath Ciomadul volcanic system. The two-
 178 dimensional computational domain consists of a 60 km by 60 km section, where the upper 40 km
 179 represents the crust according to Hauser et al. (2007) and the remaining 20 km represents the upper
 180 mantle. Ciomadul volcanic system is idealized as having a 25 km upper-mid crust consisting of
 181 amphibolite facies metamorphic rocks and 15 km lower crust consisting of granulite facies
 182 metamorphic rocks. Initially, we assume that the crust has a steady-state geothermal gradient. The
 183 temperature profile is calculated using one-dimensional steady-state heat equation using
 184 radiogenic heating as a source term, where we assume that the radiogenic elements concentrate in
 185 the uppermost 12 km of the crust and decay exponentially with depth. We chose a temperature of

186 0°C for the surface, and a constant heat flux at the mantle-crust boundary. After calculation of the
187 geothermal gradient, the side-boundary temperatures are kept constant during the transient
188 calculations.

189 In order to quantify the magma evolution in the crust over time, we emplace dikes and sills
190 incrementally over 10^5 - 10^6 yr. Intrusion of magmas increases the temperatures of the surrounding
191 crust, while the individual intrusions cool down due to heat transfer between the crust and the
192 magma. We solve for transient heat conduction equation using latent heat as the source term. We
193 follow the fully implicit finite volume scheme described by Patankar (1980) and use the iterative
194 predictor-corrector algorithm of Voller and Swaminathan (1991). We assume that the magma
195 emplacement process is stochastic and instantaneous as the dike emplacement timescales in nature
196 (days to weeks) are much faster than the timescales that we consider in the model (10^5 - 10^6 yr). We
197 acknowledge that the internal convection is important for the differentiation history of the crustal
198 magma bodies (i.e. (Dufek and Bachmann, 2010; Petrelli et al., 2018). However, over the time and
199 length scales that we focus in the present study, we can neglect convection effects as conduction is
200 the predominant process of heat transfer (Biot number (Bi) $\ll 1$; (Carrigan, 1988)).

201 The latent heat evolution of the system during melting and crystallization is calculated using the
202 phase diagrams of specific compositions from experiments and parameterized solutions from the
203 rhyolite-MELTS thermodynamic software (Gualda et al., 2012). The melt fraction-temperature
204 relationship of the metamorphic lithologies are taken from experiments of (Vielzeuf and Holloway,
205 1988). The intruded magma in the lower crust is assumed basaltic in composition (Nandedkar et al.,
206 2014), and the intrusions in the upper crust are presumed dacitic (compiled from a number of
207 measurements (Gelman et al., 2013)). We follow the two-stage process described in Karakas et al.,
208 (2017). The dikes and sills of basaltic composition are emplaced first in the lower crust over 1 Myr.
209 Following this lower crustal magma emplacement, heat distribution in the crust is calculated and
210 dacitic magma is then emplaced in the upper crust with intermediate to low fluxes (10^{-4} to 10^{-3}

211 km³/yr) for 500 kyr between 7 and 15 km depths, and assuming constant heat flux between the
212 lower and upper crust. This allows us to calculate the thermal evolution as well as the melt evolution
213 in the upper crust and to compare our results with the electrical conductivity, petrology, and
214 magnetotelluric studies conducted in the Ciomadul Volcanic System.

215

216 **2.3. *In situ* measurements of the electrical conductivity**

217 Samples were cold pressed to form 5-mm diameter cylindrical pellets and drilled in the center
218 leaving a 1-mm diameter hole. They were then inserted in a piston cylinder assembly modified for
219 *in situ* electrical conductivity measurements (Laumonier et al., 2017b, 2015; Sifré et al., 2014): the
220 sample is sandwiched by alumina disks to reduce the chemical contamination and surrounded by a
221 platinum foil being the external electrode. The internal electrode is a 1-mm diameter platinum wire
222 inserted in the sample hole, in contact with the B-type thermocouple that was alternatively used to
223 read the temperature right above the sample and to measure the sample resistance. Typical MgO,
224 pyrex and talc were used to complete $\frac{3}{4}$ or $\frac{1}{2}$ inch assembly according to the desired pressure.

225

226 The sample electrical resistance was measured by an impedance gain phase analyzer Solartron and
227 a 4-wire electrical set up adapted to the low resistance of hydrous silicate glasses. Resistance
228 measurements were performed during heating and cooling paths, once the temperature was stable
229 and with the thermocouple unplugged to avoid interferences with the electrical circuit. If the
230 temperature differed by more than 5°C before and after the resistance measurement, it was
231 repeated to reduce the uncertainty on the temperature. The electrical conductivity of the samples
232 was calculated from their resistance and their geometry, resulting in a typical error smaller than 0.2
233 log unit in conductivity (S/m) (Laumonier et al., 2015). The retrieved electrical conductivity is a
234 property of the melt being size-independent and that can directly be compared to the geophysical
235 estimations of electrical conductivity in the crust beneath Ciomadul volcano.

236

237 3. Results

238 3.1. Petrology of the Ciomadul dacite

239 Mineral-scale petrological studies of the erupted products of Ciomadul provide constraints on the
240 storage conditions prior to the latest eruption. Within the phenocryst assemblage, plagioclase and
241 amphibole are the dominant minerals and occur in similar relative amounts.

242 Two generations of compositionally homogeneous plagioclase are present in the youngest dacite:

243 (i) phenocryst-sized plagioclase with a spongy to sieved texture and occasional thin rim overgrowth

244 of clear plagioclase; (ii) microphenocryst-sized plagioclase without resorption feature and a clear

245 inner structure. In spite of the textural difference, both plagioclase phases have similar, relatively

246 homogeneous chemical compositions ($An = 40-50$ mol% and $FeO = 0.2-0.3$ wt%). Intergrowth of

247 both types of plagioclases with amphibole is fairly common. Amphiboles show various zoning

248 patterns and cover a wide compositional range (Appendix A) that distinguishes three groups: low

249 Al-Mg ($Al^{iv} < 1.4$, i.e. $Al_2O_3 < 10$ wt%; $MgO < 14$ wt%) hornblende, high Al-Mg ($Al^{iv} > 1.4$, i.e. $Al_2O_3 > 10$

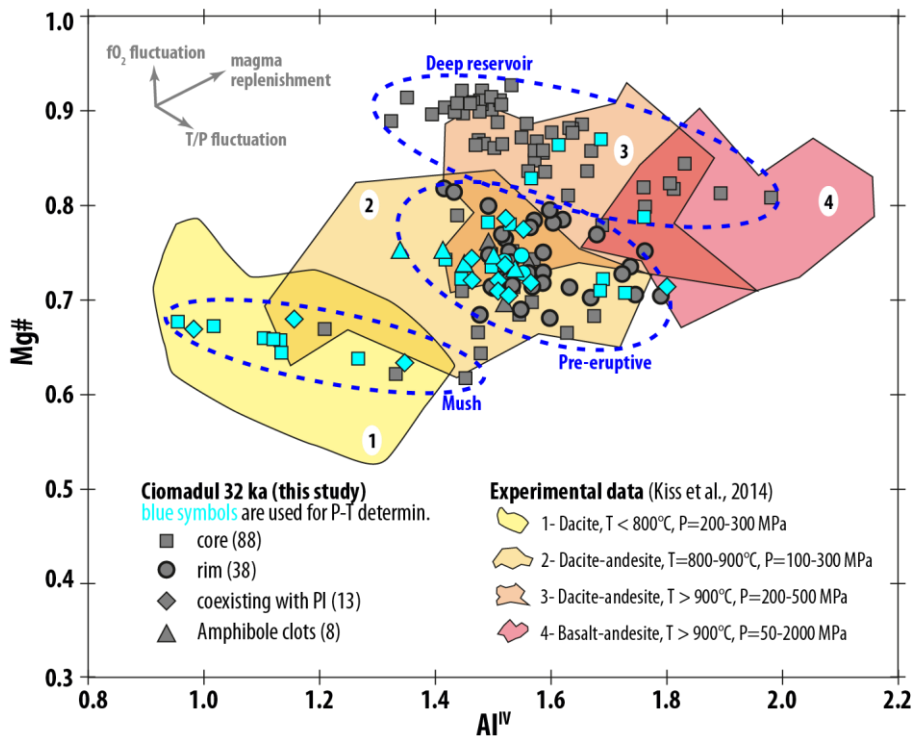
250 wt%; $MgO > 16$ wt%) pargasite/Mg-hastingsite and an intermediate group ($Al^{iv} > 1.4$, i.e. $Al_2O_3 > 10$

251 wt%; $MgO = 13-16$ wt%) (Fig. 3). Noteworthy, the intermediate composition amphibole occurs

252 always at the outer zone of the phenocrysts and appears to be in equilibrium with the erupted melt.

253 They are also found in amphibole crystal clots with interstitial glass.

254



255

256 **Figure 3: Three compositional amphibole populations distinguished in the youngest dacite used in this study** (symbols
 257 distinguish crystal cores and rims as well as amphiboles coexisting with plagioclase; numbers of analysis are indicated
 258 in parenthesis): low temperature and pressure (“mush”), high-temperature and high-pressure crystallization conditions
 259 (“deep reservoir”) and, noteworthy, amphibole rim always falling into the intermediate-temperature amphibole group
 260 (“pre-eruptive conditions”). P-T conditions from phase equilibrium experiments (yellow to red fields) are shown as
 261 compiled by Kiss et al. (2014).

262

263 3.2. Thermobarometry

264 Pressure and temperature of the magma storage can be determined using the amphibole and
 265 plagioclase compositions (Anderson et al., 2008; Holland and Blundy, 1994) on coexisting mineral
 266 pairs or using single amphibole compositions (Féménias et al., 2006; Mutch et al., 2016; Ridolfi et
 267 al., 2010; Ridolfi and Renzulli, 2012). However, the accuracy of these thermobarometric results is
 268 heavily debated in the literature: Kiss et al. (2014) and Erdmann et al. (2014) suggested that the
 269 barometric calculations introduced by Ridolfi et al. (2010) and Ridolfi and Renzulli (2012) may give
 270 often erroneous result. Furthermore, the amphibole thermometer (Ridolfi et al., 2010; Ridolfi and
 271 Renzulli, 2012) often yields higher temperature than that of Holland and Blundy (1994).
 272 Gorini et al (2018) recommended special cares when using the Ridolfi and Renzulli’s
 273 thermometer (Ridolfi and Renzulli, 2012), which were followed here (Appendix A). As a result,

274 less than 15% of the amphibole compositions with $\text{Al}_2\text{O}_3 > 10$ wt% from the studied dacite sample
275 passed the criteria and were acceptable for thermobarometric calculation (Appendix A). The
276 pressure determination is also discussed with care due to the additional effect of melt composition
277 on the amphibole chemistry (Erdmann et al., 2014; Kiss et al., 2014) (Fig. 3). For the low-Al ($\text{Al}_2\text{O}_3 < 8$
278 wt%) amphiboles, we used the geobarometry as proposed by Mutch et al. (2016) along with the
279 thermometer of Holland and Blundy (1994). Such amphiboles are often coexistent with plagioclase,
280 K-feldspar, quartz, biotite, apatite and Fe-Ti oxides in the dome rocks (Kiss et al., 2014), a requisite
281 for application of this barometry. On the other hand, the Ridolfi and Renzulli (2012)'s
282 thermobarometric calculation was used with the modification as suggested by Gorini et al. (2018)
283 for the high-Al ($\text{Al}_2\text{O}_3 > 10$ wt%) amphiboles.

284 Based on the methodology described above, we obtained temperatures above 900°C and pressure
285 from 230 to 420 MPa for the high-Al amphiboles. The low-Al amphiboles yield temperature between
286 720°C and 780°C and a pressure between 210 and 280 MPa. Noteworthy, we obtained a lower
287 temperature of 715 +/- 20°C using low-Al amphibole and plagioclase pair thermometry (Holland and
288 Blundy, 1994) for felsic clots found in lava dome rocks (Kiss et al., 2014). This is consistent with a
289 crystal mush condition with more evolved melt (represented by interstitial glasses in felsic crystal
290 clots and glass inclusions in plagioclase phenocrysts) residing at near-solidus, low-temperature
291 environment (Appendix B). The intermediate amphiboles could have crystallized at similar pressure
292 as the low-Al amphiboles, but at higher temperature (and from a slightly more mafic melt);
293 plagioclase coexisting with intermediate-Al amphibole and Fe-Ti oxide thermometry (Appendix C)
294 provide crystallization temperature of 815 +/- 20°C. We note that despite large uncertainties in the
295 accuracy of most of these thermobarometers, this is a conservative estimate. We use the
296 temperature conditions of the low Al and intermediate amphibole populations (715 and 815°C
297 respectively) to determine the water content in the melt at depth.

298

299 3.3. Determination of water concentration

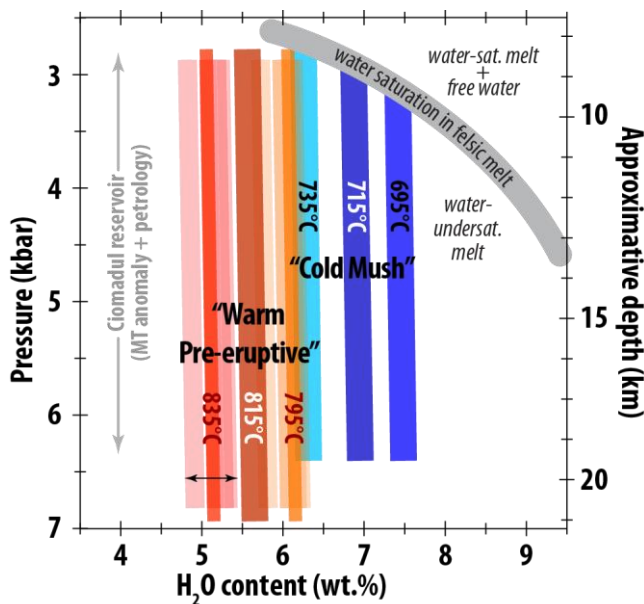
300 Using the pre-eruption thermobarometric results, the water content of the melt was estimated
 301 using the plagioclase-liquid hygrometer as calibrated by Waters and Lange (2015). Plagioclase
 302 phenocrysts have fairly homogeneous composition in the studied Ciomadul dacite (An = 40-50
 303 mol%; Appendix D), irrespective of their textural occurrence. Such variation in plagioclase
 304 composition has a poor effect on the water content calculation (+/- 0.1 wt.%; Table 2). Similarly, the
 305 pressure variation determined from petrological data (200 to 500 MPa) has a direct effect on the
 306 water saturation but no significant influence on the calculated water content (+/- 0.1 wt.%; Table
 307 2), whereas the temperature affects it by +/- 0.5 wt.% (Table 2; Fig. 4; Appendix E). Plagioclase
 308 coexisting with intermediate-Al amphibole crystallized prior to eruption under relatively elevated
 309 storage temperature (815 +/- 20°C) yields melt water contents ranging from about 4.7 to 6.3 wt%
 310 assuming melt composition represented by the interstitial glass in amphibole clots and amphibole
 311 glass inclusions. (Table 2; Fig. 4; Appendix E). At low temperature (i.e., ~715 +/- 20°C), the
 312 crystallization of An₄₀₋₅₀ plagioclase requires water content between 7.7 and 9.0 wt.%, when using
 313 the same melt composition (Appendix A and E). However, for such near-solidus, low-temperature
 314 condition, we anticipate a more evolved melt such as shown by interstitial glasses in felsic crystal
 315 clots of the lava dome rocks, groundmass and glass inclusions in plagioclase from the pumiceous
 316 dacite. Using the composition of the interstitial glass in felsic crystal clots, representative of a felsic
 317 mush, we deduce a conservative melt water content ranging between 6.0 and 7.7 wt% (Table 2; Fig.
 318 4; Appendix A and E).

Parameter:	Temperature T	Pressure P	XAn in Plag	melt compo (wt.% SiO ₂)*	XH ₂ O in melt (wt.%)	Melt EC (Log scale)	Melt fraction
Methods:	Amphibole + Fe-Ti oxide thermobarometry	thermobarometry + geophysics	Microprobe analysis	Microprobe analysis	Plag-liq hygrometer	in situ exp.	Petrology + EC + geophysics**
COLD preferred values	715°C	400 Mpa	0.45	74.5	7.0	-0.04	0.42 +/-0.05
<i>T-XH₂O trade-off</i>	<i>+/- 20°C</i>				<i>6.4 - 7.4</i>	<i>-0.21 to 0.09</i>	<i>0.28 - 0.54</i>
<i>P-XH₂O trade-off</i>		<i>250 - 500 Mpa</i>			<i>6.9 - 7.0</i>	<i>-0.08 to -0.01</i>	<i>0.35 - 0.48</i>
<i>XAn-XH₂O trade-off</i>			<i>0.40 - 0.50</i>		<i>6.9 - 7.0</i>	<i>-0.06 to -0.04</i>	<i>0.37 - 0.47</i>
<i>Melt compo-XH₂O trade-off</i>				<i>73.3 - 75.9</i>	<i>6.8 - 7.2</i>	<i>-0.08 to -0.01</i>	<i>0.34 - 0.49</i>

Cumulated uncertainties	+/- 20°C	250 - 500 Mpa	0.40 - 0.50	73.3 - 75.9	6.0 - 7.7	-0.30 to 0.17	0.25 - 0.58
WARM preferred values	815°C	400 Mpa	0.45	69.9	5.6	0.02	0.35 +/-0.04
<i>T-XH2O trade-off</i>	+/- 20°C				5.1 - 6.1	-0.12 to 0.16	0.24 - 0.51
<i>P-XH2O trade-off</i>		250 - 500 Mpa			5.5 - 5.6	-0.01 to 0.05	0.30 - 0.43
<i>XAn-XH2O trade-off</i>			0.40 - 0.50		5.5 - 5.6	0.01 to 0.02	0.32 - 0.41
<i>Melt compo-XH2O trade-off</i>				68.6 - 71.0	5.3 - 5.7	-0.03 to 0.04	0.31 - 0.44
Cumulated uncertainties	+/- 20°C	250 - 500 Mpa	0.40 - 0.50	68.6 - 71.0	4.7 - 6.3	-0.16 to 0.22	0.20 - 0.53

319 **Table 2: conservative determination of the melt fraction in Ciomadul magmatic reservoir**

320 The “preferred values” are taken from the mean of the range of each parameter while the “cumulated uncertainties”
 321 correspond to the conservative water concentration and melt fraction estimations by cumulating uncertainties. *Melt
 322 composition from natural sample to assess the water content with hygrometer of Waters and Lange (2015). In the Table
 323 is presented SiO₂ variation only. **Considering the uncertainty +/- 0.05 log unit on the electrical anomaly and using melt
 324 composition of the Ciomadul dacite. Abbrev.: Xan: Anorthite content in plagioclase; melt compo: chemical composition
 325 of the melt used in the hygrometer model; XH2O: water concentration obtained by hygrometer of Waters and Lange
 326 (2015) EC: electrical conductivity.
 327



328

329 **Figure 4: Water concentration dissolved in the melt vs. pressure** estimated by the plagioclase-liquid hygrometer of
 330 Waters & Lange (2015) for the “warm” and “cold” scenarios using amphibole glass inclusion and interstitial glass in
 331 amphibole clots, and the average glass composition from felsic clots, groundmass and glass inclusions in plagioclase
 332 respectively (Appendixes B and E). The depth of Ciomadul potential magma reservoir determined from MT observation
 333 and petrological constraints is also reported, as well as the water saturation pressure in dacitic melt (Prouteau and
 334 Scaillet, 2003). Among variable parameters, the temperature is the most influent on the water content as shown by the
 335 thick curves with labeled temperature. Propagation of uncertainties in water content due to minor variations in
 336 anorthite content (An40 to An50) and melt composition is revealed by half-transparent curves and the double arrow.

337

338 3.4. Thermal evolution of melt-bearing bodies beneath Ciomadul

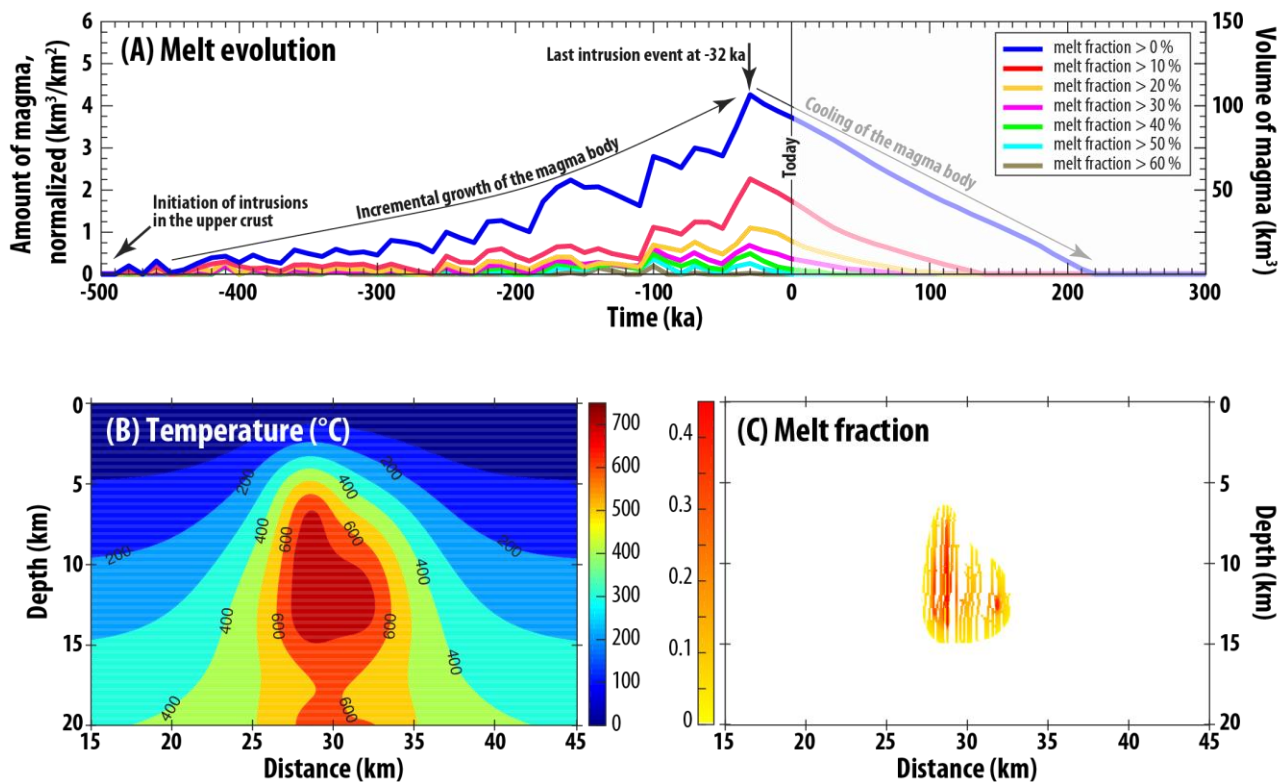
339 Our numerical results are shown in Fig. 5. The evolution of the amount of magma through time is
 340 presented from the initiation of intrusions in the upper crust, 500 kyr ago, to 300 kyr in the future

341 (Fig. 5A): numerical simulations show that existence of magma with high melt fraction (over 50%) is
342 unlikely. However, magma with 10 to 30% of melt may be relatively abundant, from about 16 to 40
343 km³. The calculated thermal state of the upper crustal magma storage is consistent with petrological
344 results and thermal calculations show that current temperature at the centre of the mush body still
345 reaches 700-750°C, allowing, locally, melt fractions up to 40% (Fig. 5B & C). These local high melt
346 fractions do not concentrate but are instead discretely distributed (Fig. 5 C).

347

348 In order to quantify the cooling timescale of the magma body, we simulated the system until it cools
349 down below its solidus under two cases. The first one implies intrusions from -500 to -32 kyr (Fig.
350 5A). To compare, the second case simulate intrusion from -500 to 0 kyr (*i.e.* till today). In both cases,
351 where we simulated different conditions (continuous intrusions vs. no intrusions) over the last 30
352 kyr, we do not observe significant differences in the temperature profile, the cooling timescale or
353 in the average melt fraction of the magma body because latent-heat buffering at high crystallinity
354 (near-eutectic conditions) maintain the system above the solidus for extended periods of time
355 (Huber et al., 2009).

356



357

358 **Figure 5: Melt and temperature in the upper crustal magma system.** (A) The upper crustal magma body grows with
 359 incremental and stochastic intrusions of magma over 470 kyr, until the last 32 ka eruption of Ciomadul. The cooling
 360 timescale is simulated by stopping magma emplacement at 470 kyr (marked as “last intrusion event”) and quantifying
 361 the volume of magma in the reservoir over time until the entire system reaches solidus. Each broken lines shows the
 362 predicted volume of magma with a certain melt fraction indicated in legend. For instance, today, numerical simulations predict about
 363 100 km³ of magma above the solidus (melt fraction > 0), and about 20 km³ of magma with more than 20% of melt. (B) Temperature
 364 profile after 500 kyr (today) in the upper magma body from numerical simulation. (C) Current melt fraction distribution
 365 from numerical simulation.

366

367 3.5. Laboratory-based determination of the dacite electrical conductivity

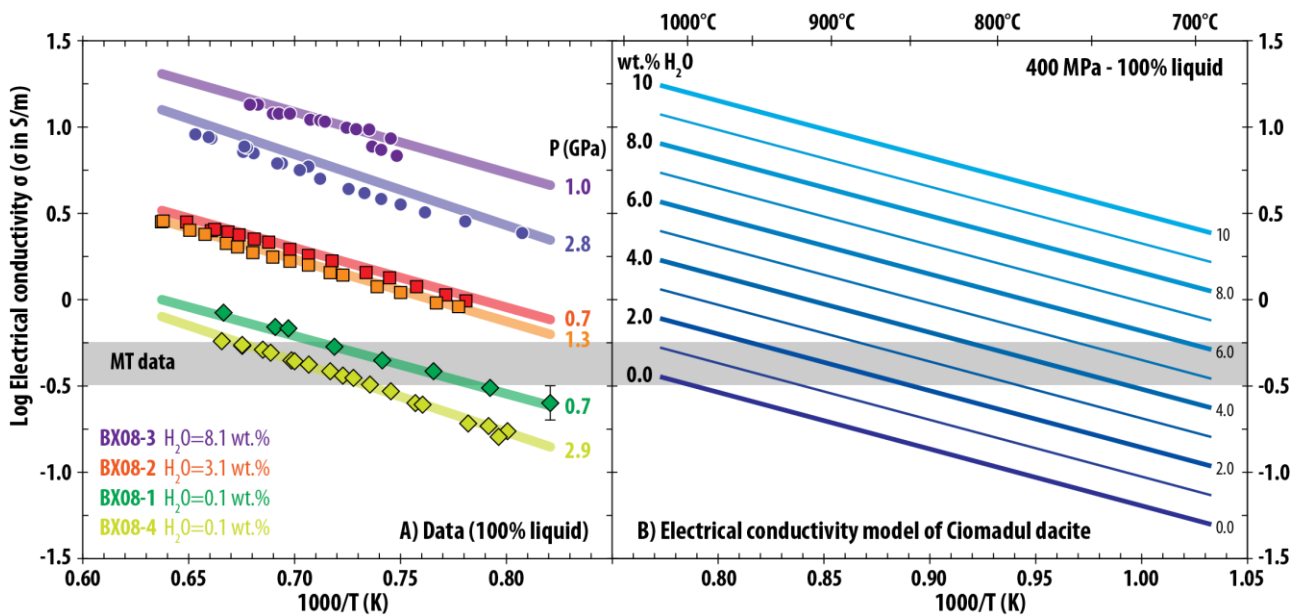
368 To verify the relevance of the thermal evolution of Ciomadul’s magmatic system determined by
 369 model calculation, we measured *in situ* the electrical conductivity of the dacite from the 32 ka
 370 Ciomadul eruption that we compare with the magnetotelluric observations of Ciomadul’s
 371 underground (Harangi et al., 2015b). Run conditions include pressures from 0.7 to 2.9 GPa, water
 372 contents from 0 to 8.1 wt.% and temperatures up to 1300°C, largely covering conditions
 373 encountered in the crust (Table 2). The results show a positive correlation of the electrical
 374 conductivity with temperature and water content, and a negative correlation with pressure typical
 375 of intermediate to felsic silicate melts (Fig. 6A). Contrary to the results found on the low Na-content

376 (2.1 wt.%) dacite from Uturuncu volcano (Laumonier et al., 2015), both activation energy and
 377 volume activation are constant here, and the effect of water on the electrical conductivity
 378 essentially reflects the evolution of the Arrhenius pre-exponential factor. The remaining variable
 379 affecting the electrical conductivity imaged by geophysical surveys is thus the melt fraction (Φ_m),
 380 which is discussed below (section 4.3).

381

Exp #	duration (h:mm)	H ₂ O (wt.%)	Pressure (GPa)	Temperature range (°C)	Activation energy (J)	Preexponential factor (S/m)
BX08-1	1:05	0.1	0.7	281	65807	164
BX08-2	1:51	3.1	1.3	230	66815	526
		3.1	0.7	280	67617	491
BX08-3	2:13	8.1	2.8	178	76417	3639
		8.1	1.1	130	66198	3021
BX08-4	0:55	0.1	2.9	247	79228	347

382 **Table 3: Sum up of experimental conditions:** duration, water content and pressure of each run as well as the
 383 temperature range used for the determination of the activation energy and pre exponential factor based on equation
 384 1.
 385



386

387 **Figure 6: Electrical conductivity data and model of the Ciomadul dacitic liquid.** (A) Reciprocal temperature vs.
 388 electrical conductivity (log scale) of the Ciomadul dacite at different water contents and pressures. Symbols are the
 389 experimental data and compared with the general model calculated for the same conditions as each data set. The
 390 grey area labeled “MT data” corresponds to the geophysical electrical conductivity anomaly identified by (Harangi et

391 al., 2015b). (B) Effect of water content, at a constant pressure of 400 MPa, on electrical conductivity of the Ciomadul
392 dacite liquid as a function of the reciprocal temperature.

393

394 4. Discussion

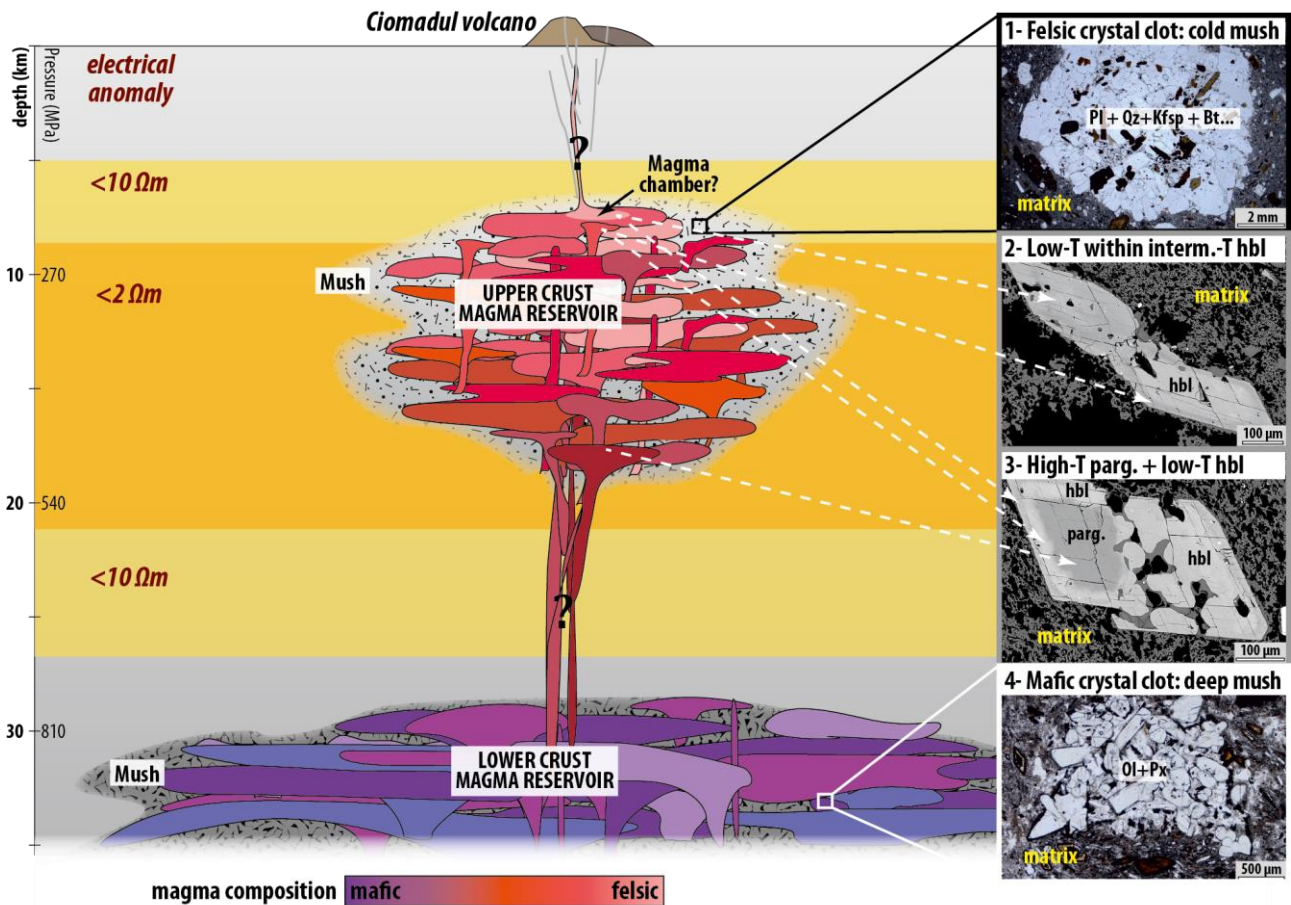
395 4.1. Magma storage conditions beneath Ciomadul

396 **Figure 7** shows the interpretative anatomy of the Ciomadul plumbing systems based on the
397 petrology of the erupted products. The high-Al and high-Mg-pargasitic amphiboles are inferred to
398 derive from a relatively deep (300-550 MPa, *i.e.* 10-18 km depth) part of the upper crustal magma
399 storage at relatively high temperature (>900°C; **Fig. 3 & 7**), and were transported to the shallow
400 depth during recharge events. There are no quantitative petrologic constraints about deeper
401 crystallization conditions, *i.e.*, above 550 MPa, although occurrence of Mg-rich minerals and crystal
402 clots involving olivine, clinopyroxene and orthopyroxene in the dome rocks suggests that less
403 differentiated basaltic magmas are also involved in the magma genesis (Kiss et al., 2014; Vinkler et
404 al., 2007). Such primitive phase assemblages could mirror magmatic processes at the crust-mantle
405 boundary or in the lower crust, akin to the MASH Zone of Hildreth and Moorbath (1988) or to the
406 hot zone of Annen et al. (2006).

407 The low-Al amphiboles (hornblendes) and plagioclases imply a relatively shallow (<300 MPa
408 pressure / 5-9 km depth), low-temperature (700-760°C) silicic mushy magma storage. The low
409 temperature conditions calculated from amphibole and plagioclase pairs are supported also by the
410 zircon and titanite temperature results, which give range from 660 to 730°C (using $a_{\text{TiO}_2} = 0.6$ and
411 $a_{\text{SiO}_2} = 1$ and the thermometers of Ferry and Watson (2007) and Watson et al. (2006), respectively).
412 Fragments of this near-solidus felsic crystal mush are represented by crystal clots with interstitial
413 evolved glass composition in the dome rocks.

414 The intermediate group of amphibole accompanied with plagioclase reveals similar depth as the
415 low-temperature hornblendes, but has higher crystallization temperature (815°C +/- 20). Textural

416 evidences suggest that this could represent conditions prior to the last eruption of Ciomadul.
 417 Texture and the temperature of the Fe-Ti oxides imply that they could have re-equilibrated with the
 418 low-T melt and their compositions preserved during the rapid magma ascent. Such features suggest
 419 that within the felsic mush body, melt-rich zones with higher temperature existed, presumably after
 420 recharge events potentially leading to the development of eruptible magma pockets.



421

422 **Figure 7: Petrological and magnetotelluric inference for the transcrustal magma plumbing system beneath Ciomadul.**
 423 The presence for a lower crustal mafic magma storage is demonstrated by mafic crystal clots (4) found in erupted
 424 products consisting of high-Mg olivine (Ol) and clinopyroxene (Px) and low resistivity anomaly at the periphery of the
 425 upper crustal magma reservoir (see Fig. 8c in (Harangi et al., 2015b)). Such mafic magmas differentiate and yield evolved
 426 magmas that rise through the crust, and cool down to build up an upper crustal felsic magma reservoir. At this stage, it
 427 is uncertain whether there is a continuous mushy magma storage between the lower and upper reservoirs. Locally, the
 428 upper magma reservoir could contain relatively high melt fraction resulting in potential magma chambers that feed
 429 volcanic eruptions. The cold mush state in the upper crustal reservoir is represented by felsic crystal clots (1) made of
 430 plagioclase (Pl), quartz (Qz), K-feldspar (Kfsp), biotite (Bt) and accessory minerals as well as amphiboles (hornblende)
 431 consistent with a temperature slightly above the solidus. Complex amphibole textures (2 and 3) indicate crystallization
 432 at different temperature and pressure and mixing of magma batches with distinct compositions suggesting a polybaric
 433 structure of the magma reservoir. The electrical anomaly identified by geophysical investigations is consistent with
 434 petrological deductions for the upper crustal reservoir (Harangi et al., 2015b).
 435

436 In summary, we infer a vertically extended (from ~5 km to ~18 km) felsic magma storage underlain
437 by a hot zone of mafic magma accumulation from the crust-mantle boundary (~40 km) up to ~30
438 km depth (Fig. 7). Mafic minerals such as olivines, clinopyroxenes and orthopyroxenes with high Mg-
439 numbers (>0.85) call for the role of mafic recharge originating from deeper in the system (Fig. 7).
440 However, we lack so far of evidence that would constrain the connection of a potential lower crustal
441 mafic reservoir with the upper one (the latter being responsible for the observed electrical
442 conductivity anomaly). Magma batches from this root zone ascend to the upper part of the magma
443 storage and occasionally mix with the more evolved magmas. These fresh magmas locally heated
444 and partially melted the crystal assemblage and transported high-Al amphiboles (pargasites/Mg-
445 hastingsites) formed at higher temperature (>900°C) and at greater depth into the shallow felsic
446 crystal mush zone. Following magma recharge, the magma condition stabilized at ~800°C, where the
447 rims of the amphiboles were formed and the Fe-Ti oxides re-equilibrated. This implies that before
448 the latest eruption, the magma storage was thermally heterogeneous, comprising both low- and
449 intermediate temperature zones that fed the eruption, as well as deeper high-temperature zones.
450 The upper part of the felsic crystal mush zone could have resided at relatively low temperature
451 (<750°C) for a prolonged (>>100 ka) period as shown by U-Th dates of zircons (Harangi et al., 2015a).
452 The depth range of the felsic upper crustal magma storage is consistent with the magnetotelluric
453 low-resistivity anomaly (Harangi et al., 2015b). Based on the monotonous chemical and petrologic
454 natures of Ciomadul dacites over the past 1 Myr (Molnár et al., 2018; 2019), one can expect similar
455 storage conditions over time.

456

457 **4.2. Definition of an electrical conductivity model for the Ciomadul dacite**

458 The electrical conductivity of the dacite melt follows the Arrhenius law:

459
$$\sigma_{dacite} = \sigma_0 \cdot \exp^{-(Ea+P\Delta V)/RT} \quad \text{(eq. 1)}$$

460 where σ_0 is a pre exponential factor ($S.m^{-1}$), E_a the activation energy (J), P the pressure (bar), ΔV the
461 activation volume ($cm^3.mol^{-1}$), R the gas constant and T the temperature (K). σ_0 can be modelled by
462 4 parameters a to d in the equation established by Laumonier et al. (Laumonier et al., 2017b, 2015):

$$463 \quad \sigma_0 = \exp\{(aw + b) + P * (cw + d)\} \quad (\text{eq. 2})$$

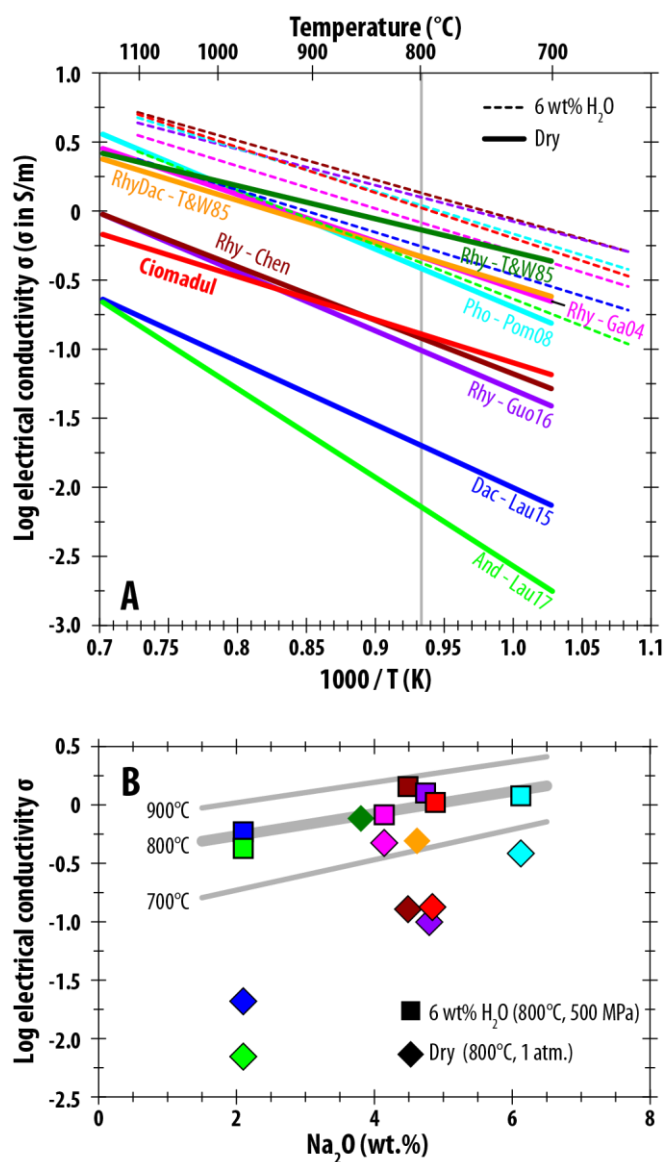
464

465 where w is the water concentration in wt.% and P is the pressure in bars. The fitting parameters are
466 $a = 0.395 \pm 0.077$; $b = 4.65 \pm 0.26$; $c = -1.77E-06 \pm 3.04E-07$ and $d = 3.91E-05 \pm 1.24E-05$.
467 Contrary to previous empirical model determined for intermediate magmas from Cerro Uturuncu,
468 (Laumonier et al., 2017b, 2015), activation energy and the activation volume were found to be
469 constant here ($E_a = 60,000 \pm 3,000 J.mol^{-1}$; $\Delta V = 6.54 \pm 1.41 cm^3.mol^{-1}$). The fitted values a to d ,
470 E_a and ΔV returned a correlation coefficient of 0.99. The effect of temperature and water content
471 is illustrated at 400 MPa in Fig. 6B.

472

473 Under dry conditions, the activation energy of the Ciomadul dacitic melt (60 kJ) is lower than the
474 one of Uturuncu dacite (88 kJ), and better resembles the one of felsic compositions that contain
475 similar sodium content (*e.g.* rhyodacite (Tyburczy and Waff, 1985) with $E_a = 59$ kJ; or a
476 rhyolite (Gaillard, 2004) $E_a = 65$ kJ; Fig. 8). Based on the existent literature, the conductivity of dry
477 intermediate to felsic melts varies over 2 orders of magnitude whereas it extends over 0.5 log unit
478 under hydrous conditions (at 800°C, Fig. 8A). It positively correlates with temperature and water
479 content, and negatively with pressure as other intermediate to felsic silicate melts (Chen et al., 2018;
480 Gaillard, 2004; Guo et al., 2016; Laumonier et al., 2017b, 2015; Pommier et al., 2008; Tyburczy and
481 Waff, 1985) (Fig. 8). Plotted against the sodium content, the electrical conductivity of felsic dry melts
482 scatters while the one of hydrous melts defines a positive trend with increasing sodium content (Fig.
483 8B). In other words, the electrical conductivity of hydrous melts corresponding to a large number of
484 magma reservoirs in the upper to middle crust (100 and 500 MPa) strongly depends on the sodium

485 content. Therefore, we agree with the previous works concluding that sodium is the main charge
 486 carrier and the key controller of the electrical behaviour of dacitic and felsic melts in general (Chen
 487 et al., 2018; Gaillard, 2004; Gaillard and Marziano, 2005; Guo et al., 2016; Laumonier et al., 2015;
 488 Pommier et al., 2008).
 489



490
 491 **Figure 8: Comparison of calculated electrical conductivity of Ciomadul dacite with data from literature.** (A) Electrical
 492 conductivity (log scale) is plotted according to the reciprocal temperature of dry ($P = 1 \text{ atm.}$) and hydrous ($P = 500 \text{ MPa}$)
 493 intermediate to felsic melts. Hydrous melts (dotted lines) and dry melts (continuous lines) respect the same color code
 494 (Chen et al., 2018; Gaillard, 2004; Guo et al., 2016; Laumonier et al., 2017b, 2015; Pommier et al., 2008; Tyburczy and
 495 Waff, 1985). (B) Electrical conductivity (log scale) at 800°C (symbols and thick curve) as a function of the sodium content
 496 (same color legend as in A). The effect of temperature on the EC of the Ciomadul dacite is shown by the thin curves
 497 labeled 700 and 900°C .
 498

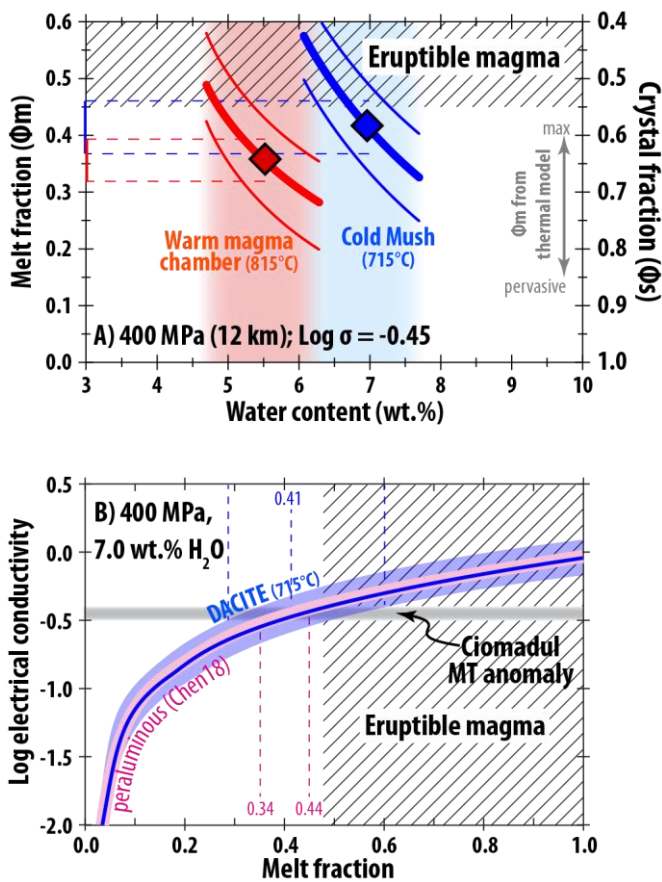
499 4.3. Determination of the melt fraction beneath Ciomadul

500 The numerical results predict the likely persistence of significant amounts of melt (up to ~40 %)
501 locally under the Ciomadul volcano and a cooling timescale of the present-day Ciomadul reservoir
502 of ~250 kyr (Fig. 5), a relatively long timescale even for a magmatic system of limited size. Such
503 prediction are confronted to the melt fraction determined from geophysical observations and the
504 electrical model: for both the relatively low-temperature crystal mush and warmer magma chamber
505 conditions, we calculated the melt fraction - water content pairs that solve the electrical
506 conductivity anomaly identified beneath Ciomadul volcano(Harangi et al., 2015b) ($\text{Log } \sigma = -0.45$).
507 The melt fraction of the magma was calculated using the modified Archie's law(Glover et al., 2000)
508 with the electrical conductivity of the dacite determined here as conductive phase and the value
509 0.001 S.m^{-1} as the solid, resistive phase, corresponding to plagioclase, amphiboles or pyroxene
510 crystals(Maury, 1968) or warm silicate rocks(Hashim et al., 2013). The exponent $m = 1.05$ in the
511 modified Archie's law was taken after Gaillard & Iacono-Marziano(Gaillard and Marziano, 2005).
512 Due to the relatively large amount of melt (more than few percents), the conductivity of the solid
513 phase has no significant effect, the liquid conductivity being the determinant one(Laumonier et al.,
514 2017a).

515

516 We find that the melt fraction ranges from ~0.20 to 0.58 (Fig. 9A). In detail, the melt fraction inferred
517 for both warm (0.35 ± 0.04) and cold (0.42 ± 0.05) scenarios explain the geophysical observations
518 (Table 2), highlighting the primary effect of water on the electrical conductivity of such a magmatic
519 system; both preeruptive and long-storage conditions produce similar electrical signatures. The
520 water content (6.0-7.7 wt.%) deduced for the low-temperature crystal mush is relatively close to
521 the water saturation pressure of dacitic melts (Prouteau and Scaillet, 2003) at the depth of the
522 geophysical anomaly; this is consistent and plausible in the case of a mushy magma that partially
523 crystallized and concentrated the water in the melt. Our melt fraction estimations would be

524 underestimated if CO₂ were present, because CO₂ decreases the amount of water in the volatile
 525 phase, and thus indirectly the electrical conductivity (Iacono-Marziano et al., 2012; Ni et al., 2011).
 526 If the residual liquid had, however, a rhyolitic rather than a dacitic composition, as deduced from
 527 glasses in felsic crystal clots and glass inclusions hosted by minerals equilibrated at relatively shallow
 528 conditions (715°C), then, it would impact on the estimation of the melt fraction using electrical
 529 conductivity. These glasses have a peraluminous composition determined from the aluminum
 530 saturation index (Appendix B), which is similar to the rhyolitic melts that were electrically
 531 characterized by Chen et al. (Chen et al., 2018). Under similar conditions (400 MPa, 7.0 wt.% H₂O),
 532 the peraluminous rhyolite is as conductive as the dacite and the pervasive melt fraction would be
 533 the same (0.34 to 0.44) to explain the geophysical anomaly (Log σ = -0.4 to -0.5; Fig. 9B).
 534



535
 536 **Figure 9: Melt fraction beneath Ciomadul volcano.** (A) The melt fraction and water content respecting the electrical
 537 anomaly (Log electrical conductivity -0.45) observed by magnetotelluric survey (Harangi et al., 2015b) for both reservoir
 538 and mush cases. The curves are truncated according to the possible range of water content constrained by the petrology

539 of the Ciomadul dacite, providing the likely range of melt fraction in the upper crust reservoir. Diamond symbols show
540 the “preferred values” presented in Table 2. The “eruptible magma” field corresponds to melt fraction higher than 0.45
541 resulting in remobilisable magma (Cooper & Kent, 2014). (B) Electrical conductivity vs. melt fraction of the Ciomadul
542 dacite and a peraluminous rhyolite (Chen et al., 2018) similar to the glass observed in Ciomadul felsic crystal clots.

543

544 Melt fractions deduced from numerical simulations are lower than the values determined from
545 electrical conductivity measurements: the calculated average melt fraction (0.14) of the magma
546 body corresponds to electrical conductivities about Log -0.6. Such average melt fraction pervasively
547 distributed cannot explain the current electrical anomaly (Harangi et al., 2015b). However, the
548 heterogeneous melt distribution predicted by the numerical model (Fig. 5) with regions with higher
549 melt fraction (up to 0.40) distributed in the magma body is a plausible explanation for the electrical
550 anomaly as deduced experimentally. Whatever the configuration, both numerical and experimental
551 approaches consistently show that a reservoir with significant content of hydrous melt could still
552 exist beneath Ciomadul volcano, despite its long dormancy and its moderate reservoir size.

553

554 **4.4. Extinct, long-dormant and potentially active volcanoes**

555 By combining petrologic observations, geophysical results, experimental conductivity data of its last
556 volcanic products and thermal modelling for the development of its magma storage, we are able to
557 decipher the present-day nature of the subvolcanic magmatic plumbing system beneath the long-
558 dormant Ciomadul volcano. Although it is generally considered as extinct (last eruption is ca. 30 ka),
559 the significant average melt fraction determined in the upper crustal magma storage makes the
560 volcano still potentially active. This conclusion is supported also by CO₂ degassing (over 10,000
561 tonnes/year emission flux) with isotopic composition implying a strong magmatic component (Kis
562 et al., 2019). Based on magnetotelluric reconstruction (Harangi et al., 2015b) of the current upper
563 crustal magma reservoir, the thermal evolution of the system and experimental constraints from
564 electrical conductivity measurements, the total volume of the upper crustal melt-bearing mush

565 beneath Ciomadul nowadays could be of the order of 100 km^3 , with a melt volume from ~ 15 up to
566 58 km^3 based on numerical and experimental determinations. Such volume exceeds the estimated
567 volume of magma involved during the development of the entire volcanic complex (Szakács et al.,
568 2015) ($8\text{-}14 \text{ km}^3$), meaning that most of magma transferred to the upper crust has not erupted. The
569 likely persistence of melt and the existence of local high melt fractions within a relatively cold mush
570 support the theory of magma storage for prolonged (> 10 's kyr) periods above the solidus
571 (Szymanowski et al., 2017) Such condition could characterize not only the active and potentially
572 active volcanoes, but also other seemingly inactive volcanoes, worldwide.

573 Although (1) a volcano is generally considered as extinct when its quiescence period exceeds 10 kyr
574 and (2) we cannot predict an upcoming eruption at Ciomadul, we show that determining the state
575 of a volcano and evaluating the associated potential hazard is critical, and must be performed
576 primarily by characterizing the nature of the subvolcanic magma storage condition. Ciomadul is not
577 a unique case; the development of remote observation techniques permits the detection of
578 geophysical anomalies beneath emblematic long-dormant volcanoes. The best example is the
579 Yellowstone, where the last eruption occurred 70 ka, yet it lies above a massive magma reservoir
580 with significant amount of melt (Huang et al., 2015). The Cerro Uturuncu in Bolivia erupted last time
581 270 ka (Sparks et al., 2008), but recent uplift and seismicity imply an active subvolcanic magma
582 storage, which was detected also by geophysical methods (Comeau et al., 2016). A slow
583 rejuvenation of the magma system beneath Colli Albani in Italy was also proposed (Iacono Marziano
584 et al., 2007), despite its last eruption occurred around 20-36 ka. The presence of significant melt
585 fraction beneath Ciomadul and other long-dormant volcanoes does not imply imminent eruption,
586 but shows that these volcanoes pose a potential and underrated threat to the population unaware
587 of the volcanic risk close by. The term, volcanoes with potential active magma storage (PAMS
588 volcano) could emphasize their importance.

589

590 **5. Conclusions**

591 With a multidisciplinary approach, we characterize the magmatic system of Ciomadul, a seemingly
592 inactive volcano at eastern-central Europe. Petrology and thermobarometry on amphiboles from a
593 32 ka lava dome dacite (one of the latest eruption products) reveals three main conditions of
594 crystallization: (1) low pressure and temperature ($\sim 715^{\circ}\text{C}$) corresponding to a mushy upper crust
595 reservoir, (2) relatively warm ($>900^{\circ}$) and deep conditions that we attribute to the deeper part of
596 the mushy reservoir and (3) intermediate conditions ($\sim 815^{\circ}\text{C}$) typical of all amphibole rims that we
597 attribute to pre-eruptive conditions at the shallow level. This dominantly felsic upper crustal mushy
598 magma storage is underlain by a hot lower crustal zone with mafic magma accumulation. Such
599 features demonstrate the transcrustal magmatic system beneath Ciomadul and were used to run
600 numerical simulation about its thermal evolution. The simulations predict the slow cooling of
601 the upper reservoir and the persistence of at least 15% of melt (locally reaching up to 40%). We
602 finally tested these predictions by performing experiments on the dacite with in situ electrical
603 conductivity measurements. We find that the geophysical anomaly identified beneath Ciomadul can
604 be explained by an upper crustal magma reservoir, which contains between 20 and 58% of nearly
605 water-saturated dacitic to rhyolitic melt. Such thermal evolution and presence of melt is consistent
606 with a magma storage existing for a protracted time (around 350 kyr; (Harangi et al., 2015a) and
607 supports the hypothesis of long-lasting, persistent magma storage above the solidus (Szymanowski
608 et al., 2017). From experiments and thermal calculations, we demonstrate here that Ciomadul
609 magmatic system could locally contain significant amount of melt with relative fraction close to the
610 eruptible state in some regions. Such magma storage conditions can exist even beneath relatively
611 small volcanic complexes. As long as melt-bearing magma body can be inferred beneath such long-
612 dormant volcanoes, the potential for rejuvenation exists, irrespective of the length of its quiescence
613 time and this calls for more attention to apparently inactive PAMS volcanoes.

614

615 **Acknowledgements**

616 This project was supported by ERC #279790 and ANR #2010 BLAN62101 projects attributed to FG;
617 OTKA-NKFIH K116528 (SH) and NKFIH PD 121048 (RL) research grants. OK and OB acknowledge the
618 support from SNF Grant #200021_178928. ML acknowledges the French Government Laboratory of
619 Excellence initiative (ClerVolc contribution number 341). IS benefited by a grant of the Ministry of
620 Research and Innovation, CNCS-UEFISCDI, project PN-III-P4-ID-PCCF-2016-0014, within PNCDI III.
621 We thank C. Miller and M. Petrelli for their reviews that greatly clarified the paper.

622
623 **References**

- 624 Anderson, J.L., Barth, A.P., Wooden, J.L., Mazdab, F., 2008. Thermometers and thermobarometers
625 in granitic systems. *Rev. Mineral. Geochemistry* 69, 121–142.
- 626 Annen, C., Blundy, J.D., Sparks, R.S.J., 2006. The genesis of intermediate and silicic magmas in deep
627 crustal hot zones. *J. Petrol.* 47, 505–539. <https://doi.org/10.1093/petrology/egi084>
- 628 Bachmann, O., 2010. The petrologic evolution and pre-eruptive conditions of the rhyolitic Kos
629 Plateau Tuff (Aegean arc). *Open Geosci.* 2, 270–305.
- 630 Bachmann, O., Huber, C., 2016. Silicic magma reservoirs in the Earth's crust. *Am. Mineral.* 101,
631 2377–2404.
- 632 Barboni, M., Boehnke, P., Schmitt, A.K., Harrison, T.M., Shane, P., Bouvier, A.-S., Baumgartner, L.,
633 2016. Warm storage for arc magmas. *Proc. Natl. Acad. Sci.* 113, 13959–13964.
- 634 Bedrosian, P.A., 2007. MT+, integrating magnetotellurics to determine earth structure, physical
635 state, and processes. *Surv. Geophys.* 28, 121–167.
- 636 Carrigan, C.R., 1988. Biot number and thermos bottle effect: Implications for magma-chamber
637 convection. *Geology* 16, 771–774.
- 638 Cashman, K. V, Sparks, R.S.J., Blundy, J.D., 2017. Vertically extensive and unstable magmatic
639 systems: a unified view of igneous processes. *Science* (80-.). 355, eaag3055.
- 640 Chen, J., Gaillard, F., Villaros, A., Yang, X., Laumonier, M., Jolivet, L., Unsworth, M., Hashim, L.,
641 Scaillet, B., Richard, G., 2018. Melting conditions in the modern Tibetan crust since the
642 Miocene. *Nat. Commun.* 9. <https://doi.org/10.1038/s41467-018-05934-7>
- 643 Christopher, T.E., Blundy, J., Cashman, K., Cole, P., Edmonds, M., Smith, P.J., Sparks, R.S.J., Stinton,
644 A., 2015. Crustal-scale degassing due to magma system destabilization and magma-gas
645 decoupling at Soufrière Hills Volcano, Montserrat. *Geochemistry, Geophys. Geosystems* 16,
646 2797–2811.
- 647 Comeau, M.J., Unsworth, M.J., Cordell, D., 2016. New constraints on the magma distribution and
648 composition beneath Volcán Uturuncu and the southern Bolivian Altiplano from
649 magnetotelluric data. *Geosphere* 12, 1391–1421.
- 650 Cooper, K.M., 2019. Time scales and temperatures of crystal storage in magma reservoirs:
651 implications for magma reservoir dynamics. *Philos. Trans. R. Soc. A* 377, 20180009.
- 652 Cooper, K.M., 2015. Timescales of crustal magma reservoir processes: insights from U-series
653 crystal ages. *Geol. Soc. London, Spec. Publ.* 422, SP422-7.
- 654 Costa, F., 2008. Residence times of silicic magmas associated with calderas. *Dev. Volcanol.* 10, 1–
655 55.
- 656 Dufek, J., Bachmann, O., 2010. Quantum magmatism: Magmatic compositional gaps generated by

657 melt-crystal dynamics. *Geology* 38, 687–690. <https://doi.org/10.1130/G30831.1>

658 Erdmann, S., Martel, C., Pichavant, M., Kushnir, A., 2014. Amphibole as an archivist of magmatic
659 crystallization conditions: problems, potential, and implications for inferring magma storage
660 prior to the paroxysmal 2010 eruption of Mount Merapi, Indonesia. *Contrib. to Mineral.
661 Petrol.* 167, 1016.

662 Féménias, O., Mercier, J.-C.C., Nkono, C., Diot, H., Berza, T., Tatu, M., Demaiffe, D., 2006. Calcic
663 amphibole growth and compositions in calc-alkaline magmas: Evidence from the Motru Dike
664 Swarm (Southern Carpathians, Romania). *Am. Mineral.* 91, 73–81.

665 Ferry, J.M., Watson, E.B., 2007. New thermodynamic models and revised calibrations for the Ti-in-
666 zircon and Zr-in-rutile thermometers. *Contrib. to Mineral. Petrol.* 154, 429–437.

667 Gaillard, F., 2004. Laboratory measurements of electrical conductivity of hydrous and dry silicic
668 melts under pressure. *Earth Planet. Sci. Lett.* 218, 215–228.

669 Gaillard, F., Marziano, G.I., 2005. Electrical conductivity of magma in the course of crystallization
670 controlled by their residual liquid composition. *J. Geophys. Res. Solid Earth* 110.

671 Gelman, S.E., Gutiérrez, F.J., Bachmann, O., 2013. On the longevity of large upper crustal silicic
672 magma reservoirs. *Geology* 41, 759–762.

673 Glover, P.W.J., Hole, M.J., Pous, J., 2000. A modified Archie’s law for two conducting phases. *Earth
674 Planet. Sci. Lett.* 180, 369–383.

675 Gualda, G.A.R., Ghiorso, M.S., Lemons, R. V., Carley, T.L., 2012. Rhyolite-MELTS: a modified
676 calibration of MELTS optimized for silica-rich, fluid-bearing magmatic systems. *J. Petrol.* 53,
677 875–890.

678 Guo, X., Zhang, L., Behrens, H., Ni, H., 2016. Probing the status of felsic magma reservoirs:
679 Constraints from the P–T–H₂O dependences of electrical conductivity of rhyolitic melt. *Earth
680 Planet. Sci. Lett.* 433, 54–62.

681 Harangi, S., Lenkey, L., 2007. Genesis of the Neogene to Quaternary volcanism in the Carpathian-
682 Pannonian region: Role of subduction, extension, and mantle plume. *Spec. Pap. Soc. Am.* 418,
683 67.

684 Harangi, S., Lukács, R., Schmitt, A.K., Dunkl, I., Molnár, K., Kiss, B., Seghedi, I., Novothny, Á.,
685 Molnár, M., 2015a. Constraints on the timing of Quaternary volcanism and duration of
686 magma residence at Ciomadul volcano, east–central Europe, from combined U–Th/He and U–
687 Th zircon geochronology. *J. Volcanol. Geotherm. Res.* 301, 66–80.

688 Harangi, S., Molnár, M., Vinkler, A.P., Kiss, B., Jull, A.J.T., Leonard, A.G., 2010. Radiocarbon dating
689 of the last volcanic eruptions of Ciomadul volcano, Southeast Carpathians, eastern-central
690 Europe. *Radiocarbon* 52, 1498–1507.

691 Harangi, S., Novák, A., Kiss, B., Seghedi, I., Lukács, R., Szarka, L., Wesztergom, V., Metwaly, M.,
692 Gribovszki, K., 2015b. Combined magnetotelluric and petrologic constrains for the nature of
693 the magma storage system beneath the Late Pleistocene Ciomadul volcano (SE Carpathians).
694 *J. Volcanol. Geotherm. Res.* 290, 82–96.

695 Hashim, L., Gaillard, F., Champallier, R., Le Breton, N., Arbaret, L., Scaillet, B., 2013. Experimental
696 assessment of the relationships between electrical resistivity, crustal melting and strain
697 localization beneath the Himalayan–Tibetan Belt. *Earth Planet. Sci. Lett.* 373, 20–30.

698 Hauser, F., Raileanu, V., Fielitz, W., Dinu, C., 2007. Seismic crustal structure between the
699 Transylvanian Basin and the Black Sea , Romania 430, 1–25.
700 <https://doi.org/10.1016/j.tecto.2006.10.005>

701 Hildreth, W., Moorbath, S., 1988. Crustal contributions to arc magmatism in the Andes of central
702 Chile. *Contrib. to Mineral. Petrol.* 98, 455–489.

703 Holland, T., Blundy, J., 1994. Non-ideal interactions in calcic amphiboles and their bearing on
704 amphibole-plagioclase thermometry. *Contrib. to Mineral. Petrol.* 116, 433–447.

705 Huang, H.-H., Lin, F.-C., Schmandt, B., Farrell, J., Smith, R.B., Tsai, V.C., 2015. The Yellowstone

706 magmatic system from the mantle plume to the upper crust. *Science* (80-). 348, 773–776.

707 Huber, C., Bachmann, O., Dufek, J., 2011. Thermo-mechanical reactivation of locked crystal
708 mushes: Melting-induced internal fracturing and assimilation processes in magmas. *Earth*
709 *Planet. Sci. Lett.* 304, 443–454.

710 Huber, C., Bachmann, O., Manga, M., 2009. Homogenization processes in silicic magma chambers
711 by stirring and mushification (latent heat buffering). *Earth Planet. Sci. Lett.* 283, 38–47.

712 Iacono-Marziano, G., Morizet, Y., Le Trong, E., Gaillard, F., 2012. New experimental data and semi-
713 empirical parameterization of H₂O-CO₂ solubility in mafic melts. *Geochim. Cosmochim. Acta*
714 97, 1–23. <https://doi.org/10.1016/j.gca.2012.08.035>

715 Iacono Marziano, G., Gaillard, F., Pichavant, M., 2007. Limestone assimilation and the origin of
716 CO₂ emissions at the Alban Hills (Central Italy): Constraints from experimental petrology. *J.*
717 *Volcanol. Geotherm. Res.* 166, 91–105. <https://doi.org/10.1016/j.jvolgeores.2007.07.001>

718 Ismail-Zadeh, A., Matenco, L., Radulian, M., Cloetingh, S., Panza, G., 2012. Geodynamics and
719 intermediate-depth seismicity in Vrancea (the south-eastern Carpathians): current state-of-
720 the art. *Tectonophysics* 530, 50–79.

721 Karakas, O., Degruyter, W., Bachmann, O., Dufek, J., 2017. Lifetime and size of shallow magma
722 bodies controlled by crustal-scale magmatism. *Nat. Geosci.* 10, 446.

723 Karakas, O., Dufek, J., 2015. Melt evolution and residence in extending crust: Thermal modeling of
724 the crust and crustal magmas. *Earth Planet. Sci. Lett.* 425, 131–144.

725 Karátson, D., Wulf, S., Veres, D., Magyari, E.K., Gertisser, R., Timar-Gabor, A., Novothny, Á., Telbisz,
726 T., Szalai, Z., Anechitei-Deacu, V., 2016. The latest explosive eruptions of Ciomadul (Csomád)
727 volcano, East Carpathians—A tephrostratigraphic approach for the 51–29 ka BP time interval.
728 *J. Volcanol. Geotherm. Res.* 319, 29–51.

729 Kis, B.M., Caracausi, A., Palcsu, L., Baciú, C., Ionescu, A., Futó, I., Sciarra, A., Harangi, S., 2019.
730 Noble gas and carbon isotope systematics at the seemingly inactive Ciomadul volcano
731 (Eastern-Central Europe, Romania): evidence for volcanic degassing. *Geochemistry, Geophys.*
732 *Geosystems.*

733 Kiss, B., Harangi, S., Ntaflos, T., Mason, P.R.D., Pál-Molnár, E., 2014. Amphibole perspective to
734 unravel pre-eruptive processes and conditions in volcanic plumbing systems beneath
735 intermediate arc volcanoes: a case study from Ciomadul volcano (SE Carpathians). *Contrib. to*
736 *Mineral. Petrol.* 167, 986.

737 Laumonier, M., Farla, R., Frost, D.J., Katsura, T., Marquardt, K., Bouvier, A.S., Baumgartner, L.P.,
738 2017a. Experimental determination of melt interconnectivity and electrical conductivity in
739 the upper mantle. *Earth Planet. Sci. Lett.* 463, 286–297.
740 <https://doi.org/10.1016/j.epsl.2017.01.037>

741 Laumonier, M., Gaillard, F., Muir, D., Blundy, J., Unsworth, M., 2017b. Giant magmatic water
742 reservoirs at mid-crustal depth inferred from electrical conductivity and the growth of the
743 continental crust. *Earth Planet. Sci. Lett.* 457, 173–180.
744 <https://doi.org/10.1016/j.epsl.2016.10.023>

745 Laumonier, M., Gaillard, F., Sifré, D., 2015. The effect of pressure and water concentration on the
746 electrical conductivity of dacitic melts: Implication for magnetotelluric imaging in subduction
747 areas. *Chem. Geol.* 418, 66–76.

748 Maury, R., 1968. Conductibilité électrique des tectosilicates. II. Discussion des résultats. *Bull. la*
749 *Soc. Fr. Mineral. Cristallogr.* 91, 355–366.

750 Molnár, K., Harangi, S., Lukács, R., Dunkl, I., Schmitt, A.K., Kiss, B., Garamhegyi, T., Seghedi, I.,
751 2018. The onset of the volcanism in the Ciomadul Volcanic Dome Complex (Eastern
752 Carpathians): eruption chronology and magma type variation. *J. Volcanol. Geotherm. Res.*
753 354, 39–56.

754 Molnár, K., Lukács, R., Dunkl, I., Schmitt, A.K., Kiss, B., Seghedi, I., Szepesi, J., Harangi, S., 2019.

755 Episodes of dormancy and eruption of the Late Pleistocene Ciomadul volcanic complex
756 (Eastern Carpathians , Romania) constrained by zircon geochronology. *J. Volcanol.*
757 *Geotherm. Res.* 373, 133–147. <https://doi.org/10.1016/j.jvolgeores.2019.01.025>

758 Mutch, E.J.F., Blundy, J.D., Tattitch, B.C., Cooper, F.J., Brooker, R.A., 2016. An experimental study
759 of amphibole stability in low-pressure granitic magmas and a revised Al-in-hornblende
760 geobarometer. *Contrib. to Mineral. Petrol.* 171, 85.

761 Nandedkar, R.H., Ulmer, P., Müntener, O., 2014. Fractional crystallization of primitive, hydrous arc
762 magmas: an experimental study at 0.7 GPa. *Contrib. to Mineral. Petrol.* 167, 1015.

763 Ni, H., Keppler, H., Behrens, H., 2011. Electrical conductivity of hydrous basaltic melts: Implications
764 for partial melting in the upper mantle. *Contrib. to Mineral. Petrol.* 162, 637–650.
765 <https://doi.org/10.1007/s00410-011-0617-4>

766 Ohlhorst, S., Behrens, H., Holtz, F., 2001. Compositional dependence of molar absorptivities of
767 near-infrared OH-and H₂O bands in rhyolitic to basaltic glasses. *Chem. Geol.* 174, 5–20.

768 Patankar, S., 1980. Numerical heat transfer and fluid flow. CRC press.

769 Petrelli, M., El Omari, K., Spina, L., Le Guer, Y., La Spina, G., Perugini, D., 2018. Timescales of water
770 accumulation in magmas and implications for short warning times of explosive eruptions.
771 *Nat. Commun.* 9, 770.

772 Pommier, A., Gaillard, F., Pichavant, M., Scaillet, B., 2008. Laboratory measurements of electrical
773 conductivities of hydrous and dry Mount Vesuvius melts under pressure. *J. Geophys. Res.*
774 *Solid Earth* 113.

775 Popa, M., Radulian, M., Szakács, A., Seghedi, I., Zaharia, B., 2012. New seismic and tomography
776 data in the southern part of the Harghita Mountains (Romania, Southeastern Carpathians):
777 connection with recent volcanic activity. *Pure Appl. Geophys.* 169, 1557–1573.

778 Prouteau, G., Scaillet, B., 2003. Experimental constraints on the origin of the 1991 Pinatubo dacite.
779 *J. Petrol.* 44, 2203–2241.

780 Ridolfi, F., Renzulli, A., 2012. Calcic amphiboles in calc-alkaline and alkaline magmas:
781 thermobarometric and chemometric empirical equations valid up to 1,130° C and 2.2 GPa.
782 *Contrib. to Mineral. Petrol.* 163, 877–895.

783 Ridolfi, F., Renzulli, A., Puerini, M., 2010. Stability and chemical equilibrium of amphibole in calc-
784 alkaline magmas: an overview, new thermobarometric formulations and application to
785 subduction-related volcanoes. *Contrib. to Mineral. Petrol.* 160, 45–66.

786 Rubin, A.E., Cooper, K.M., Till, C.B., Kent, A.J.R., Costa, F., Bose, M., Gravley, D., Deering, C., Cole,
787 J., 2017. Rapid cooling and cold storage in a silicic magma reservoir recorded in individual
788 crystals. *Science (80-)*. 356, 1154–1156.

789 Seghedi, I., Downes, H., 2011. Geochemistry and tectonic development of Cenozoic magmatism in
790 the Carpathian–Pannonian region. *Gondwana Res.* 20, 655–672.

791 Sifré, D., Gardés, E., Massuyeau, M., Hashim, L., Hier-Majumder, S., Gaillard, F., 2014. Electrical
792 conductivity during incipient melting in the oceanic low-velocity zone. *Nature* 508, 81–85.
793 <https://doi.org/10.1038/nature13245>

794 Sparks, R.S.J., Folkes, C.B., Humphreys, M.C.S., Barfod, D.N., Clavero, J., Sunagua, M.C., McNutt,
795 S.R., Pritchard, M.E., 2008. Uturuncu volcano, Bolivia: Volcanic unrest due to mid-crustal
796 magma intrusion. *Am. J. Sci.* 308, 727–769.

797 Szakács, A., 1994. Redefining active volcanoes: a discussion. *Bull. Volcanol.* 56, 321–325.

798 Szakács, A., Seghedi, I., Pécskay, Z., Mirea, V., 2015. Eruptive history of a low-frequency and low-
799 output rate Pleistocene volcano, Ciomadul, South Harghita Mts., Romania. *Bull. Volcanol.* 77,
800 12.

801 Szymanowski, D., Wotzlaw, J.F., Ellis, B.S., Bachmann, O., Guillong, M., Von Quadt, A., 2017.
802 Protracted near-solidus storage and pre-eruptive rejuvenation of large magma reservoirs.
803 *Nat. Geosci.* 10, 777–782. <https://doi.org/10.1038/ngeo3020>

- 804 Tyburczy, J.A., Waff, H.S., 1985. High pressure electrical conductivity in naturally occurring silicate
805 liquids. *Point Defects Miner.* 31, 78–87.
- 806 Vielzeuf, D., Holloway, J.R., 1988. Experimental determination of the fluid-absent melting relations
807 in the pelitic system. *Contrib. to Mineral. Petrol.* 98, 257–276.
- 808 Vinkler, A.P., Harangi, S., Ntaflos, T., Szakács, A., 2007. A Csomád vulkán (Keleti-Kárpátok)
809 horzsaköveinek kőzettani és geokémiai vizsgálata—petrogenetikai következtetések
810 (Petrology and geochemistry of the pumices from the Ciomadul volcano [Eastern
811 Carpathians]—implications for the petrogenetic processes). *Földtani Közlöny* 137, 103–128.
- 812 Voller, V.R., Swaminathan, C.R., 1991. ERAL Source-based method for solidification phase change.
813 *Numer. Heat Transf. Part B Fundam.* 19, 175–189.
- 814 Waters, L.E., Lange, R.A., 2015. An updated calibration of the plagioclase-liquid hygrometer-
815 thermometer applicable to basalts through rhyolites. *Am. Mineral.* 100, 2172–2184.
- 816 Watson, E.B., Wark, D.A., Thomas, J.B., 2006. Crystallization thermometers for zircon and rutile.
817 *Contrib. to Mineral. Petrol.* 151, 413.
818